Boundary-Layer Meteorol (2008) 128:315–338
DOI 10.1007/s10546-008-9291-0

ORIGINAL PAPER

Temporal and Spatial Variations of the Aerodynamic Roughness Length in the Ablation Zone of the Greenland Ice Sheet

C. J. P. P. Smeets · M. R. van den Broeke

Received: 24 May 2007 / Accepted: 3 July 2008 / Published online: 25 July 2008

Abstract To understand the response of the Greenland ice sheet to climate change the so-called ablation zone is of particular importance, since it accommodates the yearly net surface ice loss. In numerical models and for data analysis, the bulk aerodynamic method is often used to calculate the turbulent surface fluxes, for which the aerodynamic roughness length (z_0) is a key parameter. We present, for the first time, spatial and temporal variations of z_0 in the ablation area of the Greenland ice sheet using year-round data from three automatic weather stations and one eddy-correlation mast. The temporal variation of z_0 is found to be very high in the lower ablation area (factor 500) with, at the end of the summer melt, a maximum in spatial variation for the whole ablation area of a factor 1000. The variation in time matches the onset of the accumulation and ablation season as recovered by sonic height rangers. During winter, snow accumulation and redistribution by snow drift lead to a uniform value of $z_0 \approx 10^{-4}$ m throughout the ablation area. At the beginning of summer, snow melt uncovers ice hummocks and z_0 quickly increases well above 10^{-2} m in the lower ablation area. At the end of summer melt, hummocky ice dominates the surface with $z_0 > 5 \times 10^{-3}$ m up to 60 km from the ice edge. At the same time, the area close to the equilibrium line (about 90 km from the ice edge) remains very smooth with $z_0 = 10^{-5}$ m. At the beginning of winter, we observed that single snow events have the potential to lower z_0 for a very rough ice surface by a factor of 20 to 50. The total surface drag of the abundant small-scale ice hummocks apparently dominates over the less frequent large domes and deep gullies. The latter results are verified by studying the individual drag contributions of hummocks and domes with a drag partition model.

Keywords Ablation area · Aerodynamic roughness length · Drag partition model · Greenland Ice sheet · Ice surface roughness

C. J. P. P. Smeets (✉) · M. R. van den Broeke
Institute for Marine and Atmospheric Research Utrecht, Princetonplein 5, 3584 CC Utrecht, The Netherlands
e-mail: c.j.p.p.smeets@uu.nl

1 Introduction

Next to the Antarctic ice sheet, the Greenland ice sheet constitutes the second largest ice mass on earth. Although the potential of melting of the Greenland ice sheet to increase global sea level is smaller than the Antarctic (approximately 7 against 62 m), it is situated in a warmer climate and therefore possibly more susceptible to global warming. Recent observations indicate a rapidly increasing ice-sheet mass deficit during the last decade (Alley et al. 2005; Rignot and Kanagaratnam 2006; Velicogna and Wahr 2006). Ablation, for the Greenland ice sheet, is about equally divided between ice calving and surface run-off (calving is the breaking off of a mass of ice from the ice front or ice shelf). Along the margin of the Greenland ice sheet, a 40–100 km wide melt or ablation zone is found where most of the summer melt occurs. In this paper, we particularly focus on this ablation zone because of its importance for the response of the Greenland ice sheet to climate change.

Surface melting is controlled by the surface energy balance that is primarily divided between radiation and turbulent fluxes. In the ablation area, the contributions of the sensible and latent heat fluxes to surface melt relates as 4:1 and can be up to 35% of the net energy balance. In numerical models or for the analysis of automatic weather station (AWS) data, the turbulent surface flux is usually calculated with the bulk aerodynamic method. The aerodynamic roughness length (z_0) is one of the key input parameters for this method, and the spatial and temporal variations of z_0 in the ablation zone are the main subject of this study.

Very little is known about the variations of z_0 in the Greenland ablation area, and most model studies adopt a constant value in space and time. Micrometeorological observations from the lower ablation zone are scarce due to the crevassed and hummocky ice surface that makes access difficult. Meteorological experiments, providing detailed information on z_0, have therefore mostly been performed well above 1,000 m.a.s.l., on the flat and smooth surface near the equilibrium line, and on single locations during summer over (melting) snow. Examples are the French EGIG (Expédition Glaciologique Internationale au Groenland) expeditions to west Greenland in 1957–1960 and 1967–1968 (Ambach 1977a, b), the experiments by the ETH Zürich in 1991 and 1992 (Eidgenössische Technische Hochschule Zürich, Forrer and Rotach 1997), the experiment of the Free University of Amsterdam during GIMEX91 (Greenland Ice Margin Experiment, Meesters et al. 1997), and the KABEG expedition during spring in 1997 (Katabatic Wind and Boundary Layer Front Experiment around Greenland, Heinemann and Falk 2002). These experiments reported that z_0 varied between 10^{-3} and 10^{-4} m.

The GIMEX expeditions in 1991 and 1992 were the first attempts to study the spatial variability of the ablation zone climate during summer (Oerlemans and Vugts 1993, see Fig. 1. The Institute for Marine and Atmospheric Research Utrecht (IMAU) and the Free University of Amsterdam used four meteorological stations on the ice, ranging from the low ablation area to the equilibrium line, along the so-called K-transect. The GIMEX experiments provided the first studies of z_0 variations in the lower ablation area during summer (Duynkerke and Van den Broeke 1994; Van den Broeke 1996), though the results were inconclusive, with a large variation of z_0 between 8×10^{-4} and 0.12 m. Since GIMEX in 1990, the IMAU has performed continuous mass balance measurements and, ongoing from the mid-nineties, operated several AWS in this area (Van de Wal et al. 2005). Three new AWS were installed in August 2003 at locations S5, S6 and S9 (Fig. 1). From August 2003 to August 2004, eddy-correlation measurements were performed at S6. The AWS and eddy-correlation data obtained during this period are presented here and used to derive, for the first time, the year-round variations of the aerodynamic roughness length at three locations in the ablation zone of the Greenland ice sheet.

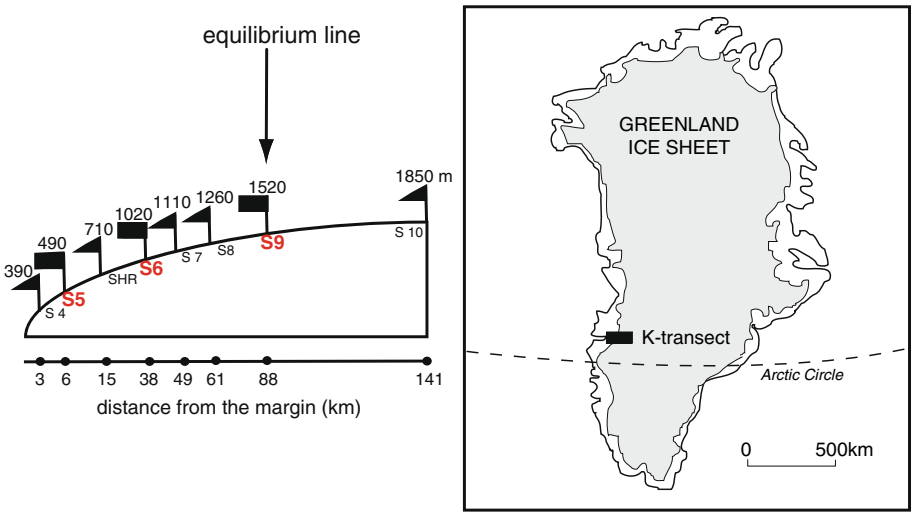

Fig. 1 The location of the K-transect in the ablation area of the West-Greenland ice sheet together with a cross-section showing the names, heights, and distance from the ice edge for each site. The AWS locations are marked red

2 Field Area and Intrumentation

2.1 Field Area

The K-transect (Fig. 1) lies near Kangerlussuaq, in south-western Greenland, just north of the Arctic Circle. The transect has been operated since 1990 and currently constitutes eight locations with mass balance and GPS measurements and three AWS. At this location, the strip of land between the ocean and ice sheet is relatively wide (100 km) and characterised by hilly tundra and the 140 km long Kangerlussuaq fjord. The large distance from the ocean leads to a low arctic and continental climate at the location of the ice edge with average winter and summer air temperatures of −18.0 and +9.3°C, respectively (Box 2002), and low annual precipitation averaging 120 mm water equivalent. The climate is extremely stable with a monthly mean of 241 sun hours from May to August. From the ice edge, at about 200 m.a.s.l., the broad gently sloping ablation area extends 90 km eastward to meet the equilibrium line at 1,520 m.a.s.l. where S9 is located. Table 1 lists yearly 2-m height averages from all three AWS.

Figure 2 shows the 30-min data of wind direction (upper panel) and wind speed/temperature (lower panel) from S6, which are representative of the other AWS locations. Throughout the year, the boundary layer is dominated by a persistent south-easterly wind that is deflected about +35 degrees from the downslope direction due to Coriolis forcing. This so-called katabatic flow implies year-round stable stratification close to the surface and a wind maximum at some distance above (Van den Broeke et al. 1994). In summer, the dominant driving force of the katabatic flow is a temperature deficit in the near-surface air caused by daytime warming of the tundra in combination with a melting ice surface (Van den Broeke et al. 1994). During winter, the forcing is dominated by the radiative cooling of the ice/snow surface (Heinemann 1999). Although the steepest slope and the largest katabatic forcing are found at S5, the year-round highest wind speeds are consistently observed at S9 as a result of synoptic forcing and

Table 1 Climatology at the AWS locations for the period August 2003 to August 2004

location	S5	S6	S9
Height (m)	490	1,020	1,520
Distance from ice edge (km)	6	38	88
Wind speed u ($\mathrm{m\,s^{-1}}$)	3.9	5.1	5.8
Temperature T (°C)	−4.1	−8.5	−11.4
Relative humidity Rh (%)	76	87	92
Specific humidity q ($\mathrm{g\,kg^{-1}}$)	2.1	1.9	1.6
Wind direction dd (°)	120	124	126
Directional constancy*	0.87	0.91	0.82

* The wind directional constancy is calculated as the ratio of the magnitudes of the average vector and absolute wind speed

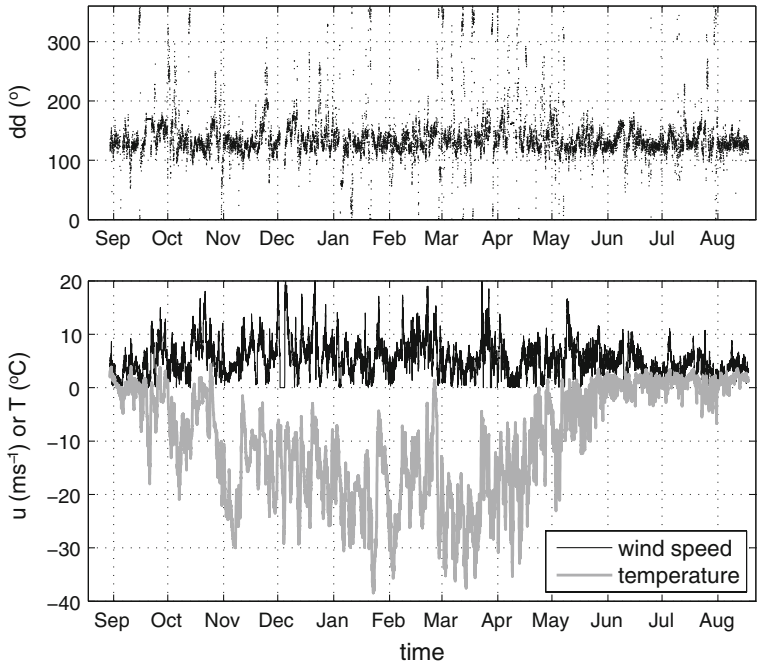

Fig. 2 Wind direction (upper panel) and wind speed/temperature data (lower panel) measured at 2-m height at location S6 as a function of time (August 2003 to August 2004)

smaller z_0. This forcing is strongest during winter (Steffen and Box 2001), causing high wind maxima around 100 m above the surface (Heinemann 1999). During summer, when synoptic forcing is less, the wind maxima are typically found at a height of several tens of m (Van den Broeke et al. 1994), and the adiabatically heated downflow leads to lower relative humidity at lower elevations (Table 1). Notice that, during summer, the temperature variations are damped due to the melting ice surface (Fig. 2).

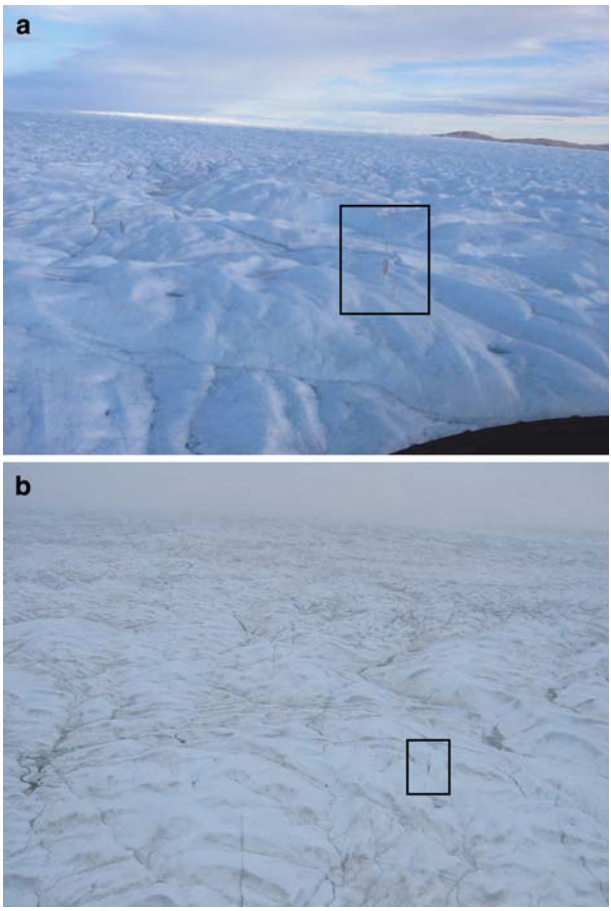

Fig. 3 Photographs of S5 taken from a helicopter at the end of the melt season: (**a**) August 2003, (**b**) August 2005. The rectangles mark the AWS, which is 6 m high

2.2 Surface Conditions at the end of the Summer

To provide an overview of the surface conditions at the three AWS locations, we describe the surface characteristics for the end of the melt season during our yearly service visit (mid-August). At this time of year, the surface roughness in the lower ablation area is at its maximum.

At S5 (Fig. 3), the surface is rough and inhomogeneous and we can distinguish two different surface obstacle scales. Figure 3a shows the abundant small ice hummocks (10–15 m wide and 0.5–2 m high) and in Fig. 3b large domes can be identified (60–120 m wide and 3–4 m high). Figure 3b clearly illustrates that the domes are homogeneously covered with hummocks.

At S6 (Fig. 4a), the surface is covered with small hummocks (average height 0.6 m) and small depressions filled with melt water. The surface is irregularly intersected with deep and wide gullies that cover about 5% of the surface area (average depths and widths are about 2 m). The location of these gullies does not change much from year to year. In Fig. 4a, part

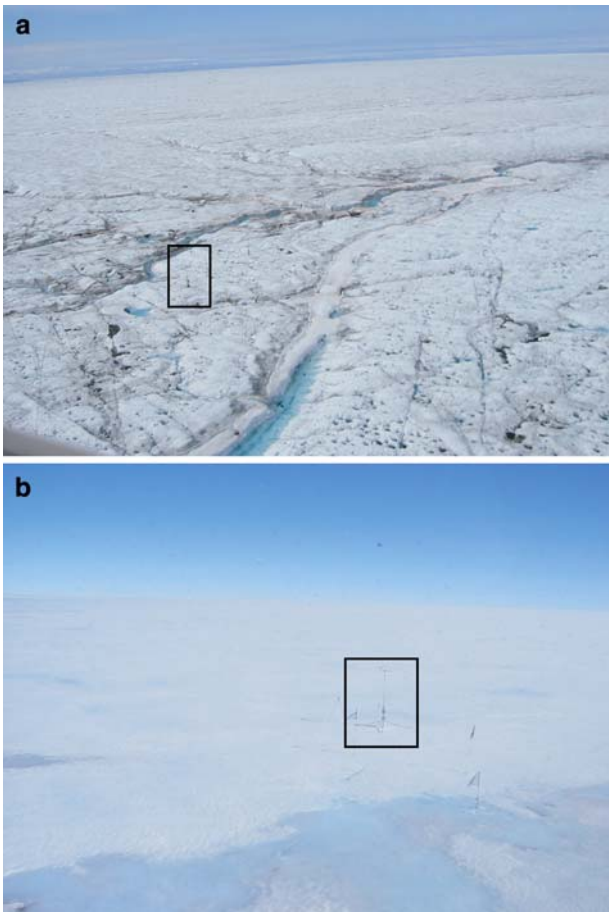

Fig. 4 Photographs of S6 and S9 taken from a helicopter at the end of the melt season: (**a**) S6 August 2004, (**b**) S9 August 2003. The rectangles mark the AWS, which is 6 m high

of the gullies is covered with remnants of snow bridges, which suggests that during winter the gullies are filled with snow and the surface becomes flat.

At S9 (Fig. 4b), the surface is flat and very smooth throughout summer and may consist of ice, snow, wet snow and/or melt water.

2.3 Instrumentation

The high summer melt rate does not allow for the use of masts that are rigidly fixed to the surface. Our two-level AWS masts (Fig. 5a) consist of a central pole and four legs that spread out from the centre making a small angle with the surface. Once placed, the legs descend about 0.5 m into the ice through melting, and are then firmly fixed. In the course of the ablation season, the masts maintain their upright position within a few degrees and the measurement height is almost constant. All measurements presented herein were performed from 30 August 2003 to 18 August 2004.

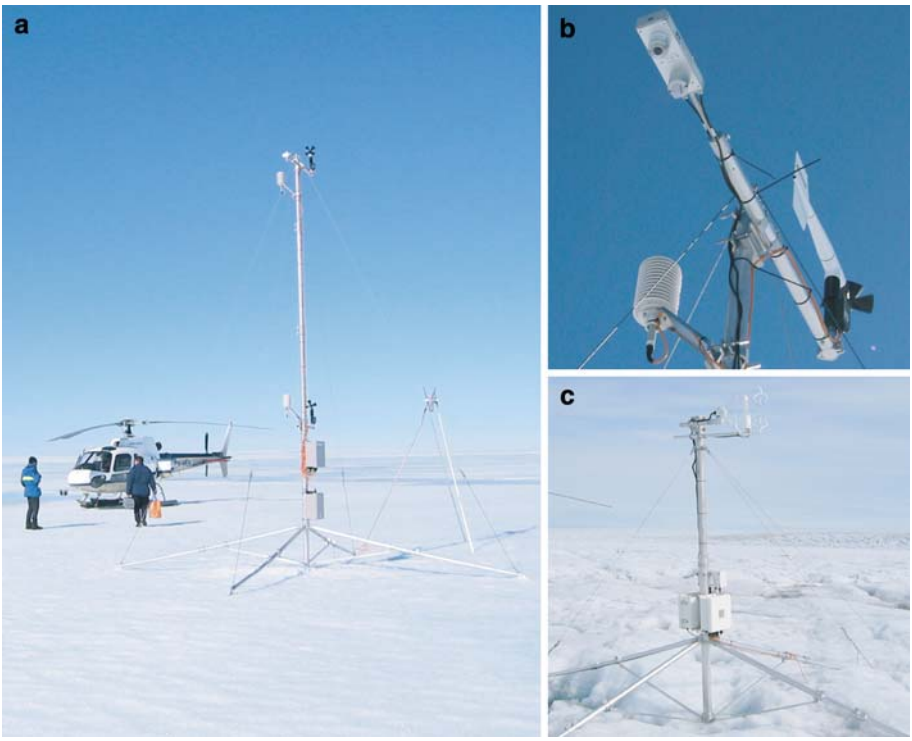

Fig. 5 (**a**) AWS mast at S9, (**b**) detail of the upper sensor boom, (**c**) turbulence mast at S6 in August 2003

In Table 2, we list the instrumentation on our AWS and eddy-correlation masts together with the specifications provided by the manufacturer. At the AWS, wind speed (u), wind direction (dd), temperature (T) and relative humidity (Rh) measurements are performed at about 2 and 6 m. The combined temperature/humidity sensors are housed in non-ventilated radiation shields. A net radiometer is mounted at 6 m height and all four radiation components are measured separately together with the radiometer body temperature. In Fig. 5b a detail of the upper boom is depicted showing the radiation, a temperature/humidity and propellor-vane sensors. Surface height measurements (z) are performed with a sonic height ranger on a separate tripod located close to the AWS (Fig. 5a, just behind the AWS). A Campbell CR10X datalogger, sampling every 30 s, stored 30-min averages.

The eddy-correlation measurements at S6 (Fig. 5c) were performed at a height of 2.75 m and consisted of the three-axial sonic wind speeds (u, v, w), the sonic temperature (i.e., an adequate approximation of the virtual temperature T_v), the thermocouple temperature (T), and the specific humidity (q). The asymmetric sonic sensor head was positioned into the prevailing wind direction. The measurement path lengths of the sonic anemometer and hygrometer are 0.10 and 0.125 m, respectively. The sensor head of the thermocouple is very small and was placed directly behind (0.05 m) the measuring volume of the sonic anemometer without significantly disturbing the flow. The hygrometer was placed next to, and 0.17 m behind, the measuring volume of the sonic anemometer. Sampling of the sonic anemometer signal was made at 10 Hz in a mode that ensures the lowest current drain. Every 10 min the mean,

Table 2 A list of all AWS and turbulence mast sensors

Variable	AWS sensor	Accuracy
u	05103-L R.M. Young	$\pm 0.3\,\mathrm{m\,s^{-1}}$
dd	05103-L R.M. Young	$\pm 3^\circ$
T	Vaisala HMP45	± 0.4°C at -20°C
Rh	Vaisala HMP45	$\pm 2\%$ (Rh$< 90\%$)
net radiation	Kipp Zonen CNR1	daily total $\pm 10\%$
z	Height ranger SR50*	$\pm 0.01\,\mathrm{m}$
Variable	**Turbulence sensor**	**Accuracy**
u, v, w	CSAT3 Sonic Anemometer*	offset error$<$ $\pm 0.04\,\mathrm{m\,s^{-1}}$
T_{sonic}	CSAT3 Sonic Anemometer*	resolution ± 0.025°C
T	FW3 Type E thermocouple*	± 0.2°C
q	LI-COR LI-7500	RMS noise $< 0.005\,\mathrm{g\,kg^{-1}}$

* Manufacturer Campbell Scientific

standard deviation and covariance values were calculated and stored on a Campbell CR23X datalogger.

3 Determining the Aerodynamic Roughness Length

In this Section, we discuss general considerations for the determination of aerodynamic roughness length and relate these to the typical conditions in the ablation area of the Greenland ice sheet, that is, a sloping surface consisting of smooth as well as very rough ice. Data selection criteria are given and the quality of the results is tested by comparing the profile and the eddy-correlation method for data from location S6.

3.1 Background Theory

The roughness of a surface describes the surface sink strength for momentum and can be defined as the integrated result of turbulent drag caused by many obstacles from small to large in size. Well above the obstacles, the flow becomes horizontally homogeneous in the so-called inertial sublayer (ISL) (Blackader and Tennekes 1968) where the Monin-Obukhov similarity theory applies (Businger et al. 1971).

In the Greenland ablation area, the surface layer is usually stably stratified and the wind speed profile can be written as

$$U(z) = \frac{u_*}{k}\left\{\ln\left(\frac{z-d}{z_0}\right) + \alpha_m \frac{(z-d)}{L}\right\}, \tag{1}$$

where $U(z)$ is the average wind speed as a function of height z, u_* is the friction velocity, z_0 is the aerodynamic roughness length, d is the zero-plane displacement, α_m is a coefficient of the stability function, k is the von Kármán constant (taken as 0.40), L is the Obukhov length defined as $L = -u_*^3\theta_v / kg\overline{w\theta_v}$ with g the gravitational acceleration, θ_v the virtual potential temperature, and $\overline{w\theta_v}$ the virtual heat or buoyancy flux. Note that the latter is well represented by the uncorrected sonic flux (Schotanus et al. 1983). The classic static stability correction $\alpha_m(z-d)/L$ is used because we only study data obtained during slightly stable

conditions, i.e. $0 < z/L < 0.1$, for which all published stability functions yield comparable values (Andreas 2002). The same reasons apply to the use of equal stability functions for momentum, temperature, and humidity.

A value for z_0 can be calculated either directly from eddy-correlation data or from the two-level AWS profile data by extrapolating the log-linear wind profile down to a height where $U = 0$. We calculate the diabatic correction term from our AWS data by using the following well-known relation (Pandolfo 1966):

$$z/L_P = Ri_g/(1 - 5Ri_g), \tag{2}$$

with

$$Ri_g = \frac{g}{T}\frac{(\partial z/\partial T)}{(\partial u/\partial z)^2}. \tag{3}$$

Later in the Section, we test the quality of the results for z_0 and z/L_P derived from our two-level AWS profiles and eddy-correlation results.

3.2 A Smooth Ice Surface

When the surface is relatively smooth (S6, S9), the surface obstacles are much smaller than the measurement height z, and the logarithmic profile (Eq. 1) is valid close to the surface floor so that d can be neglected. Similarity of wind profiles over smooth and sloping ice or snow surfaces is verified by many field experiments within at least several metres above the surface provided that atmospheric stability effects are minimal (e.g., Munro and Davies 1978; Forrer and Rotach 1997; Meesters et al. 1997; Smeets et al. 1998).

3.3 A Rough Ice Surface

When the ice surface is rough, such as at S5, the surface obstacles become comparable or larger than z (Fig. 6a) and d is an important length scale. As depicted in Fig. 6a, the actual wind profile (solid line) departs significantly from logarithmic below z_*, the height of the roughness sublayer (RSL). For $z < z_*$, the mean flow varies three dimensionally as a function of the proximity of roughness elements, implying horizontal inhomogeneity (Wieringa 1993). Extrapolating the log linear part of the wind profile towards $U(z) = 0$, we arrive well above the actual surface floor at $(d + z_0)$ (Fig. 6a, dotted line). Care has to be taken now when we analyse the wind profiles because, with the lowest sensors within the RSL, z_0 can be severely underestimated (Duynkerke and Van den Broeke 1994; Raupach et al. 1980). Smeets et al. (1999) presented measurements that were performed over a rough hummocky ice surface and found that $z_* = 2H$, where H is the average hummock height. Furthermore, above z_* similarity of the profiles was found to be valid in line with wind-tunnel data, numerical simulations over regular arrays of cubical obstacles, and observations over vegetated surfaces and urban areas (Wieringa 1993; Grimmond and Oke 1999; Castro et al. 2006; Coceal et al. 2007).

3.3.1 The Estimation of z_* and d for S5

We investigate the values of z_*, d and the height of the lowest measurement level relative to z_* at S5 for the most extreme case, that is, at the end of the melt season when all length scales related to surface roughness have their maximum values.

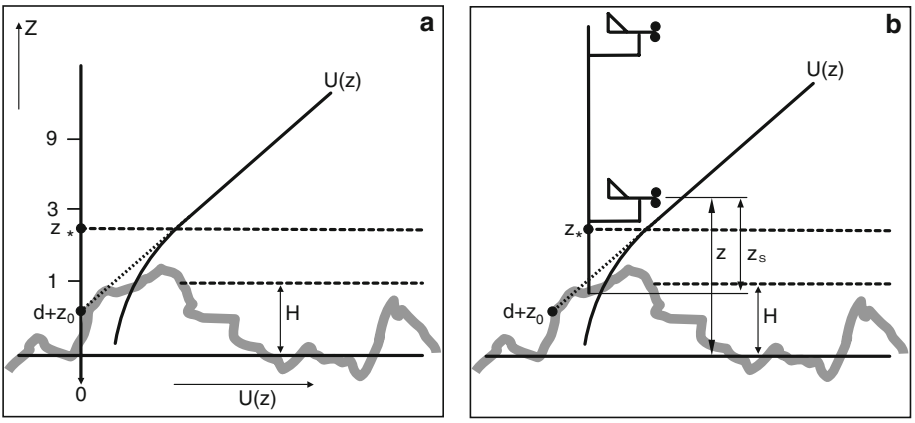

Fig. 6 Schematic representations of the (**a**) wind profile characteristics and (**b**) the AWS mast at S5 in the case of a very rough ice surface at the end of the melt season

Following Smeets et al. (1999), we assume that $z_* = 2H$. However, as discussed in Sect. 2.2, it is not straightforward to estimate a value for H at S5 since we observed two distinctly different obstacles, i.e., large domes covered with smaller and numerous hummocks. It is unclear which of these obstacles determines H. Observations at the beginning of winter (Sect. 4.3) show that z_0 is very responsive to the first snow events. With a typical magnitude of 0.1 to 0.2 m of snowfall, there is the potential to smooth the hummocks but to leave the deep and wide gullies unaltered. This suggests that the hummocks mainly determine z_0, and with that, also H. Hence, small-scale surface roughness apparently dominates momentum transfer, a result that is also evident from several other studies such as Jackson and Carroll (1978); Banke et al. (1980), Andreas et al. (1993) and Andreas (1995) over snow and Makin and Kudryavtsev (1999) in a theoretical study of momentum transfer over the ocean. To corroborate this for our data, we study the individual drag contributions from domes and hummocks with the drag partition model from Andreas (1995) (fully outlined in Appendix I). The model results (Table 3 in Appendix I) confirm that the hummocks dominate z_0 and agree quite well with our profile derived values at the end of the melt season. The latter confirms both the quality of the model calculations and the importance of hummock roughness for z_0. The average height of hummocks is estimated to be $H = 1.5$ m so that $z_* = 2H = 3$ m.

A value for d is estimated in Appendix I (Table 3) using three different methods, i.e., the drag model and results from the simplified expressions by Raupach (1994) and Shao and Yang (2005). With $H = 1.5$ m and d/H ranging between 0.66 and 0.27 we obtain a maximum of $d \approx 0.5$ m at the end of the melt season.

To determine the measurement height of the lowest sensor relative to z_* at S5 we schematically depicted all relevant length scales in Fig. 6b. The AWS was located on a hummock but in a small depression, about 0.5 m deep, so that the measurement height, relative to the surface floor of the hummocks, is $z = z_s + H - 0.5 = z_s + 1$ with $z_s = 2.6$ m the lowest sensor height relative to the local ice surface. The value of z_0 is omitted because it is relatively small. While $z_* = 3$ m, the lowest measurement height was at least 3.6 m above the surface floor and we therefore assumed that all our AWS profiles were obtained well above z_* throughout the year. The measurement height equals $(z - d) = 3.1$ m at the end of summer melt. During winter, snow accumulates in the large gullies and between the hummocks, which reduces d and H

significantly. In our calculations, we assume that the measurement height $(z - d)$ reduces linearly in time from $z = 3.1\,\mathrm{m}$ to $z_s = 2.6\,\mathrm{m}$ in winter (i.e., 1 November 2003 to 1 May 2004).

3.4 Data Selection Criteria

Good quality year round measurements are difficult to obtain in high Arctic regions. Nevertheless, the eddy-correlation and AWS sensors performed well. Less then 10% of the turbulence data at S6 were affected by snow events, riming or unknown reasons and thermocouple data were fine for more than 99% of the time. The Young propellor vane time series are continuous and clear icing effects are present for only about 2% of the time. The temperature and humidity instruments performed well with the exception of 377 spurious temperature readings at S6 during the melt season that were caused by a water related problem in one of the sensors. It seems likely that the continuous katabatic wind in the ablation area ensures ventilation of the sensors, which helps to establish such favourable statistics.

The selection criteria aim at high quality wind profiles and we select near-neutral conditions by demanding $0 < z/L < 0.1$ and $u > 5\,\mathrm{m\,s^{-1}}$. Due to the presence of persistent katabatic winds this leaves about 40% of the data and ensures that the wind speed maximum lies at least several tens of m above the surface so that this will not influence the wind profiles of the AWS. Since we only have two measurement levels at our AWS, z_0 is especially sensitive to errors in the wind gradient (see the error analysis in Appendix II). We use this sensitivity to our advantage and study $\ln(z_0)$ versus wind direction to discern a wind sector without flow disturbance by the AWS mast, sensors or the nearby sonic height ranger tripod. Non-stationary conditions were ruled out by demanding that the temperature changes between consecutive 30-min runs were less than 0.3 K (stationarity of runs can most effectively be evaluated from temperature variations; Joffre 1982). Sonic height ranger data are used to exclude all runs during and close to snowfall events. The number of 30-min runs left for the profile analysis are 2752, 2034 and 1750 for S5, S6 and S9, respectively.

The eddy-correlation measurements at S6 are subject to imperfect levelling due to the surface slope ($\approx 1°$) and variations in mast orientation during the melt season. The latter effect prohibits the use of a fixed rotation, such as the planar fit method (Wilczak et al. 2001). Instead, we force the individual 30-min averages of $\overline{v}$ and $\overline{w}$ to zero. In the case of a stationary and homogeneous boundary layer in two-dimensional and axially symmetric flow fields $\overline{v'w'}$ should equal zero, but in practice this is seldom the case. As part of the data selection criteria, we require $\left|\overline{v'w'}/\overline{u'w'}\right| < 0.25$.

Eddy-correlation measurements always underestimate turbulent fluxes as a consequence of e.g. physical limitations in sensor size and response. Sonic anemometer data are only affected by pathlength averaging between the sonic anemometer sensor heads, and we corrected for this according to Moore (1986). No corrections were applied to the sonic temperature fluxes since these represent an adequate approximation of the virtual temperature flux that is used to calculate z/L (Kaimal and Finnigan 1994). Other selection criteria for eddy-correlation data are $u_* > 0.1\,\mathrm{m\,s^{-1}}$ and $1 < \sigma_w/u_* < 1.6$. The latter criterion refers to common values found during slightly stable conditions. After selection, 1572 runs are left containing eddy-correlation and profile data for S6.

3.5 A Comparison Between AWS and Eddy-correlation Data

The AWS have two profile levels and small errors in the wind gradient result in large errors for z_0 (Langleben 1974; Wieringa 1993). This is especially true for a smooth ice or snow

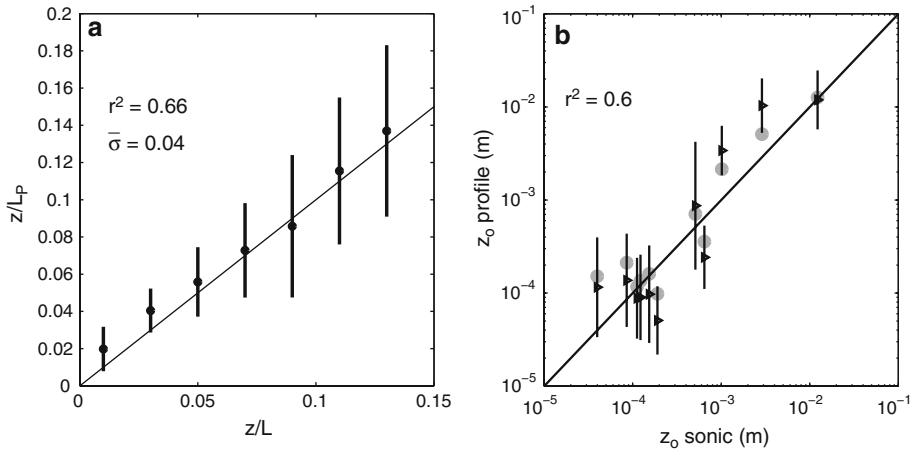

Fig. 7 (**a**) Stability parameter from sonic anemometer data (z/L) versus profile-derived values (z/L_P), (**b**) aerodynamic roughness lengths z_0 from eddy-correlation data (z_0 sonic) versus profile-derived results (z_0 profile). For profile data we apply two static stability corrections: (grey dots) z/L derived from eddy-correlation data and (black triangles) z/L_P from profile data. Each data point represents a time-binned median value with a bin size of 25 days and the error bar is the twofold standard deviation within a bin

surface for which relatively small vertical wind gradients result. In this Section we test the quality of our AWS profiles results by using the eddy-correlation data from S6.

3.5.1 Diabatic Profile Correction

Values for z/L are calculated straightforward from the eddy-correlation data and by using Eqs. 2 and 3. The vertical gradients, at the height of the sonic-anemometer (between the AWS levels), are approximated from the two AWS levels and assuming a log-linear variation with height (e.g. for wind speed $(u_2 - u_1)/[\sqrt{z_2 z_1}\ln(z_2/z_1)]$). The shielded but unventilated Vaisala temperature sensors are subject to radiation errors, and we minimized these errors by applying a correction procedure. The differences between the Vaisala and thermocouple measurements are used to tune a physical model that incorporates the wind speed and the sum of incoming and reflected shortwave radiation fluxes to explain the excess temperatures. A correction for the thermocouple excess temperatures is estimated from Jacobs and McNaughton (1994). The average temperature bias reduces from $+0.40$ to -0.03°C during summer daytime hours (i.e. shortwave incoming radiation above 200 W m^{-2}).

In Fig. 7a, we compare the results from wind profiles (z/L_p) and eddy-correlation (z/L) data using bin-averaged median values. The error bars are two-sided standard deviations within a bin. The median values scatter around the 1:1 line and, as can be expected from two-level profile data, the uncertainty increases with z/L. Nevertheless, for near-neutral conditions, Eq. 2 gives satisfactory results to estimate z/L from the AWS data.

3.5.2 Profile Versus Eddy-correlation Derived z_0

In Fig. 7b we compare z_0 values from eddy-correlation data with two different results from profile data. We apply both static stability corrections from the previous paragraph to calculate the profile results. Doing so, we distinguish between errors resulting from the wind gradient measurements and the estimate of the stability correction using Eq. 2. The results

are shown as time binned median values with a bin size of 25 days and error bars for the z/L_P corrected results (black triangles; two-sided standard deviations within a bin). Considering that we only use two-level profile data, the overall agreement is quite good and errors due to uncertainties in the wind gradient and the stability correction term are comparable. We conclude that it is possible to derive realistic aerodynamic roughness lengths from the two-level AWS wind profiles.

4 Aerodynamic Roughness Lengths in the Ablation Area

The profile derived year-round z_0 values for S5, S6 and S9 are presented. Temporal and spatial variations are discussed separately, as well as the influence of individual snow events on the variation of z_0.

4.1 Temporal Variation of z_0

In Fig. 8a and b height ranger data and bin-averaged median z_0 values for all AWS are presented as a function of time, respectively. In the lower ablation area (S5 and S6) the temporal variation of z_0 is large (a factor of 500) and the transition from summer to winter values is rapid. The variation in time matches the onset of the accumulation and ablation seasons as recovered by sonic height rangers. At the end of summer, the surface consists of hummocky ice and z_0 reaches a maximum of about 50×10^{-3} and 10×10^{-3} m at S5 and S6, respectively. The decrease of z_0 at the beginning of winter, when the first snow arrives, is surprisingly fast, which suggests that snow very effectively smoothes surface irregularities, fills in depressions and bridge gullies. During winter, accumulation and re-distribution of snow by the wind (snow drift) makes the surface aerodynamically smooth and results in a uniform value of $z_0 \approx 10^{-4}$ m throughout the ablation area.

At S9, near the equilibrium line, we observe a reversal in seasonal variation of z_0. During the summer season, surface melt at S9 consolidates the snow at the surface and removes all irregularities resulting in a very smooth surface (10^{-5} m). During winter, the drifting of snow and the continuous formation and reshaping of sastrugi (Andreas and Claffey 1995) both lead to an increase of z_0 compared to summer values (see below).

The drifting of snow is studied by plotting bin-averaged median values of z_0 versus u_* for wintertime eddy-correlation data from S6 in Fig. 9 (November 2003 to March 2004, and $T < -5°C$). The error bars are two-sided standard deviations from the bin data. As the wind speed increases, more particles are taken up by the wind and z_0 increases in line with the power law increase of z_0 expected for flow with a saltation layer, i.e., $z_0 = 0.01u_*^2/g$ (Owen 1964). These results compare very well with those obtained by Heinemann and Falk (2002) at a location about 50 km north of the K-transect at the end of winter during the KABEG experiment (their location A4 at 1,600 m.a.s.l, 75 km from the ice edge).

To judge the quality of our profile-derived z_0 values, we include an error analysis in Appendix II, which illustrates how the different errors and assumptions in the calculations contribute to the uncertainty in the year-round results. The error analysis is performed for S5 data since these are considered to be the most uncertain. In general, the error in the measurement of the wind gradient dominates the uncertainty in z_0. Only at the end of the melt season, when the surface is very rough, do the combined errors in d and z/L_P result in a comparable uncertainty. The results are evidence of the good quality of the wind gradient measurements from the AWS throughout the year.

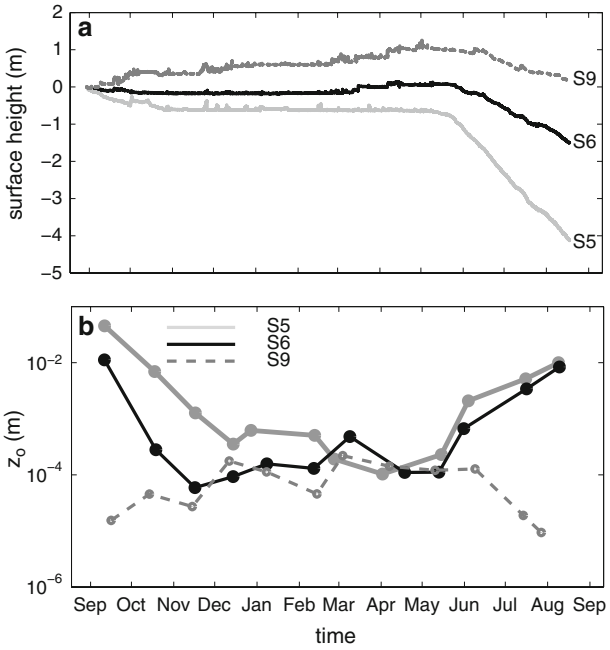

Fig. 8 (**a**) Surface height observations from the sonic height ranger, (**b**) profile-derived aerodynamic roughness lengths z_0 from S5, S6 and S9 as a function of time. Every dot represents a bin-averaged median value (bin size = 25 days)

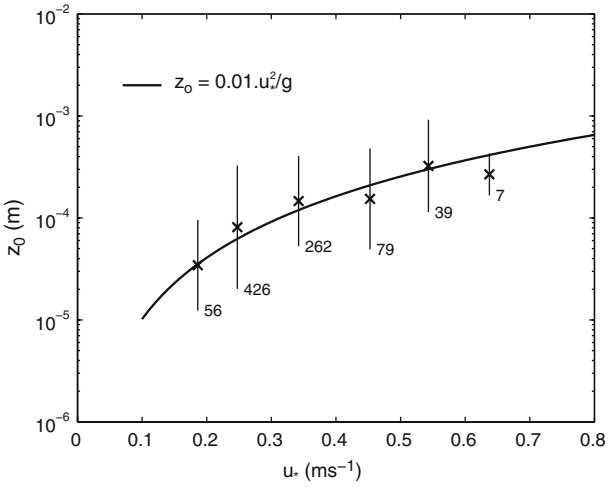

Fig. 9 The variation of z_0 as a function of u_* for wintertime data from S6 (November 2003 to March 2004, $T < -5°C$). The solid line represents the power law increase of z_0 in a flow with a saltation layer and the error bars represent the twofold standard deviation within a bin

4.2 Spatial Variation of z_0

In Fig. 10, we present the variation of z_0 as a function of distance from the ice edge during winter (December to May) and at the end of summer (September 2003 and August 2004). For the summer period, we included estimates for S7 and S8 that were calculated with the drag model using surface characteristics from photographs and observations during the yearly visits. The error bars represent two-sided standard deviations within a bin.

During winter, z_0 is almost constant throughout the ablation area (10^{-4} m) and only slightly increases when moving from S9 towards the ice edge. At the end of summer melt, the spatial variation is at its maximum and about a factor 1000 across the area. The large hummocks in the lower ablation area increase z_0 well above 10^{-2} m while, at the same time, the area close to the equilibrium line (S9) is very smooth with $z_0 = 10^{-5}$ m. It is remarkable that, up to about 60 km from the ice edge, a hummocky ice cover dominates the ablation area with $z_0 > 5 \times 10^{-3}$ m.

4.3 A Case Study of two Snow Events

The impact of the first snow events at the beginning of winter is studied in detail to illustrate their influence on z_0. In Fig. 11, time series for S5 (left panels) and S6 (right panels) of wind speed, temperature, surface height, and z_0 are presented. We only plotted above freezing temperatures (thick grey solid lines) to better identify between periods with melting and freezing. The wind speed criterium is relaxed ($U > 3\,\mathrm{m\,s^{-1}}$) to obtain a more continuous dataset. For S6, we simultaneously present sonic and profile data to illustrate the good agreement of the 30-min values of z_0.

At S5 (left panels), z_0 is large until DOY 274 when a single snow event produces about 0.2 m of fresh snow while the wind speed is low. After the event, the rapid increase of the wind speed concurs with a rapid decrease of the snow height (about 0.1 m), probably the

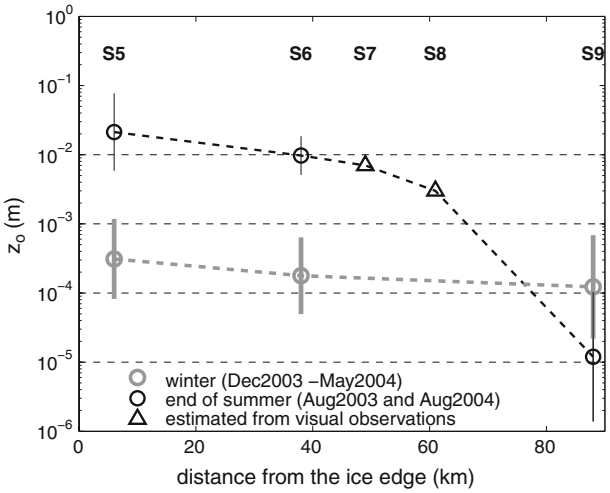

Fig. 10 Variation of z_0 as a function of distance to the ice edge. Winter values (grey) are averages for the months December to May and end of the summer values are averages from September 2003 and August 2004. The circles are the measured values from S5, S6 and S9 and the triangles are estimates for S7 and S8 using the drag model and visual interpretation of the surface during the yearly visits

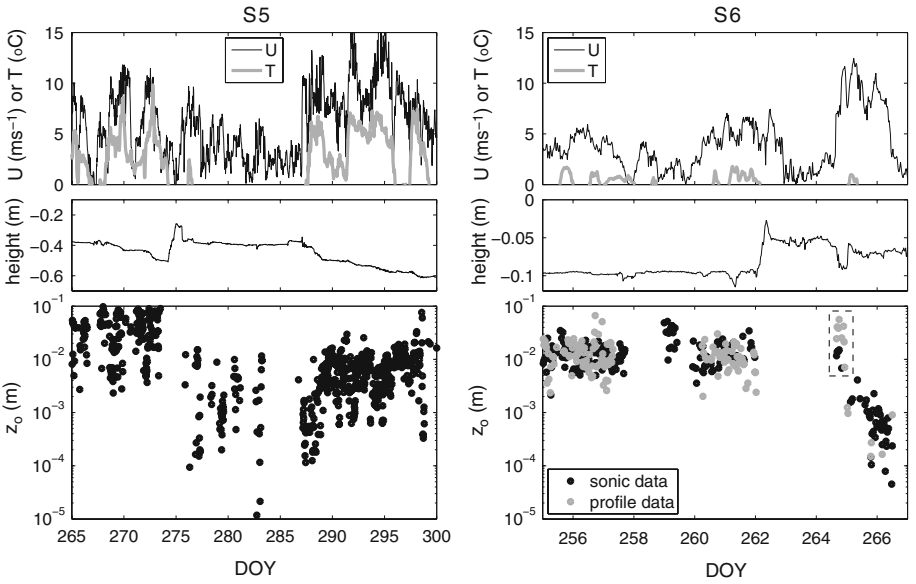

Fig. 11 Time series of snow events at S5 (left panels) and S6 (right panels). From above, the frames show wind speed and temperature, ablation/accumulation from the sonic height ranger and z_0. The dashed rectangle in the plot of z_0 for S6 marks conditions with significant snowdrift

result of snow redistribution. This process ceases during DOY 276 when melt occurs, consolidating the snow. Due to the snow event, z_0 is reduced by a factor of 50. At DOY 287 the wind increases to $10\,\mathrm{m\,s^{-1}}$ and melt causes surface lowering, a disappearing snow cover and a gradual increase of z_0.

At S6 (right panels), z_0 is large until DOY 262 with very good agreement between the sonic and profile-derived half-hourly values. During DOY 262, a snow event brings about 0.07 m of fresh snow while the air temperature is well below 0°C. During the event, the wind speed increases to $7\,\mathrm{m\,s^{-1}}$ so that snow is redistributed and the surface lowered by a few tens of mm. At DOY 263, the wind reduces to $1\,\mathrm{m\,s^{-1}}$ and the temperature falls to −25°C. At the end of DOY 264, the wind rapidly increases well above $10\,\mathrm{m\,s^{-1}}$, causing significant drifting of snow, a subsequent increase of z_0 (the data within the dashed rectangle), and rapid snow redistribution (visible as a temporary surface level variation). Shortly after the increase of the wind speed, a short period of melt occurs that consolidates the snow and prevents drifting. At that time, z_0 is a factor of 20 lower than before the snow event.

We conclude that single snow events with only about 0.1 m of fresh snow have the potential to lower z_0 of a very rough surface by a factor of 20 to 50. This supports our claim in Sect. 3.3 that the small-scale hummocks at S5 control z_0. The amount of snow involved is simply too little to influence the large domes and gullies.

5 Conclusions

We present, for the first time, year-round values of the aerodynamic roughness length (z_0), a key parameter in the bulk aerodynamic method, at three locations in the ablation area of the Greenland ice sheet. The data were obtained using three AWS and one eddy-correlation

mast. Two AWS were located in the lower ablation area and one at the equilibrium line at roughly 500, 1,000, and 1,500 m.a.s.l., respectively.

First, we verified the good quality of the z_0 results from the two-level AWS profiles by comparing them to eddy-correlation results. The temporal variations of z_0 in the lower ablation area appear to be very large (factor 500) with, at the end of the summer melt, a maximum in spatial variation throughout the ablation area of a factor 1000. The variations in time match the onset of the accumulation and ablation seasons as recovered by sonic height rangers. At the end of summer melt, hummocky ice covers the ablation area up to 60 km from the ice edge with z_0 varying from 5×10^{-3} m to well above 10^{-2} m. At the same time, the area close to the equilibrium line is very smooth with $z_0 = 10^{-5}$ m. In winter, snow accumulation and re-distribution smoothes the surface throughout the ablation area very quickly, resulting in a uniform value of about $z_0 = 10^{-4}$ m.

Surprising is the very fast decrease of z_0 in the lower ablation area at the beginning of winter. Single snow events, with only 0.1 m of fresh snow, have the potential to lower z_0 of a very rough ice surface by a factor of 20 to 50. This suggests that the total surface drag of the abundant small-scale ice hummocks dominates over the less frequent large domes and deep gullies. These results are verified by studying the individual drag contributions of hummocks and domes with a drag partition model.

Acknowledgements We would like to thank the IMAU technicians for designing and maintaining the AWS and turbulence stations, and all the people involved in the data collection. Furthermore, the comments from two anonymous referees are very much appreciated. This work is funded by the Utrecht University and the Netherlands Polar Program (NPP) of the Netherlands Organisation of Scientific Research, section Earth and Life Sciences (NWO/ALW).

Appendix I: Drag Partition Model

A drag partition model is used to calculate the individual contributions of the large domes and smaller scale hummocks to the aerodynamic roughness length z_0 for location S5. In addition, we calculate values for the displacement height d for a range of hummock geometries. The drag partition model originates from Raupach (1992) and was adapted by Andreas (1995) to specifically study the wind directional dependent drag of a field of sastrugi-like snow drifts.

The model concept is to partition the total surface stress into contributions from form drag and stress on the underlying surface. The model is based on scaling and dimensional analysis that describe the scales of surface obstacle wakes and wake interaction. The predictions include total stress, stress partition, zero-plane displacement d, and the aerodynamic roughness length z_0. Andreas (1995) shows that the model is well capable of reproducing the measured total drag and its dependence on the wind direction for a sea-ice surface covered with sastrugi. The model was also tested in a comprehensive review of geometric (or morphometric) models in Grimmond and Oke (1999) and conceptually validated by Crawley and Nickling (2002) in a wind-tunnel study. The model should be applied to cases with modest obstacle density $\lambda < 0.3$, where λ is the frontal area index representing the ratio of the frontal area of an element with the ground area occupied. For rough ice, λ varies between 0.05 and 0.15 and the model is therefore well suited for our application. For a comprehensive

description of the model we refer to the articles listed above. We now reproduce the main equations and explain the concept following Andreas (1995).

As a consequence of the persistent katabatic wind in the ablation area, our data are confined to a narrow wind sector (30°). The wind directional dependency of the model results is found to be small so that we do not include a directional dependency in the drag model equations.

The drag partition concept assumes that the total surface stress τ is partitioned into contributions from form drag τ_R and from stress on the underlying surface τ_S, so that $\tau = \tau_R + \tau_S$. In the model, the total stress τ is written as

$$\tau = \rho U_H^2 \left[C_{SH} + \lambda C_R\right] \exp\left(-c\lambda \frac{U_H}{u_*}\right) \tag{4}$$

where ρ is the air density, U_H is wind speed at height H, C_{SH} is the drag coefficient of the underlying surface referenced to a height H (i.e. the obstacle height), C_R is the form drag coefficient of the obstacle, and c is an empirical constant determined to be 0.25 by Raupach (1994). The exponential term accounts for sheltering effects by the roughness elements with c determining the rate at which an element wake spreads in the cross-stream direction. A drag coefficient referenced to a height z is directly related to z_0 through

$$C_z^{-1/2} = \frac{U(z)}{u_*} = \frac{1}{k} \ln[(z-d)/z_0]. \tag{5}$$

Notice also that the drag coefficient for the total surfaces stress, referenced to height H, can be written as

$$\tau/\rho U_H^2 = u_*^2/U_H^2 \equiv C_{DH} = 1/r^2. \tag{6}$$

Inserting this into Eq. 4 and rearranging terms we obtain

$$[c\lambda r/2]\exp(-c\lambda r/2) = [c\lambda/2][C_{SH} + \lambda C_R]^{-1/2}, \tag{7}$$

which has the form

$$Xe^{-X} = a. \tag{8}$$

Equation 8 is solved using Newton's method giving multiple solutions, and the only nontrivial case is when $0 < a < e^{-1}$, which has only one physical solution. Next, X is related to the total drag coefficient according to

$$C_{DH}^{-1/2} = 2X/c\lambda. \tag{9}$$

We now discuss the derivation of C_{SH}, C_R and λ values. To obtain C_{SH} we assume that the surface stress at S5, at the end of the melt season, relates to the roughness of a flat melting ice surface that is homogeneously covered with ice grains (microscale roughness) at the scale of mm or tens of mm. For such a surface, z_0 is found to vary around 10^{-3} m (Smeets et al. 1999; Denby and Smeets 2000). Before using this value as a model input, we first translate it into the corresponding neutral drag coefficient referenced to 10-m height

$$C_{S10} = k^2 \ln[(10-d)/z_0]^{-2} \approx 2 \times 10^{-3}. \tag{10}$$

Notice that d for a smooth melting ice surface is very small and can be neglected in Eq. 10.

To determine a value for λ, we need the scale and areal coverage of hummocks and domes. These are estimated from photographs taken from a helicopter and from surface observations during our yearly visits at the end of the melt season. A hummock is represented by a wedge

with its inclined plane directed into the wind. The average height is about $H = 1.5\,\mathrm{m}$ and its rectangular sides are $10H$ and $5H$, with the short side in line with the wind direction. A dome is represented by a cone with an average height of $H = 3.5\,\mathrm{m}$ and a radius of $15H$. Since the top of a dome is much smoother than that of a cone, the frontal area is substantially larger and increased by a factor of 1.5. The areal coverage of hummocks is about 25 per $5{,}000\,\mathrm{m}^2$, and for domes, lying adjacent to each other, it is the reciprocal of their own surface area. Hence, the unit surface area A per element is about $200\,\mathrm{m}^2$ and $8{,}660\,\mathrm{m}^2$.

We estimate C_R from the results of Banke et al. (1980), who specifically performed form drag measurements on six wedge shaped ice ridges with different slope angles of the wedge. They found a linear relationship between the inclination angle of the ice ridge and the drag coefficient $C_R = 0.012 + 0.012\alpha$ with α the slope of the inclined plane in degrees. This result was also confirmed by wind-tunnel data. We use the same relation to estimate the drag coefficient of the inclined sides of hummocks and domes at S5.

To convert the drag coefficients referenced at 10 m and H we need to know the wind speed profile. Near the top of large roughness elements, such as at S5, the log-linear profile (Eq. 1) is not valid since it will be influenced by the flow around the obstacles. To overcome this problem, a profile correction is introduced similar to the stability function. The log-linear profile near the top of the obstacles is therefore written as

$$C_{DH}^{-1/2} \equiv \frac{U_H}{u_*} = \frac{1}{k}\left[\ln\left(\frac{H-d}{z_0}\right) + \psi_H\right] \tag{11}$$

from which we can derive the result for z_0

$$z_0 = (H-d)\left[\exp(kC_{DH}^{-1/2}) - \psi_H\right]^{-1} \tag{12}$$

with ψ_H a profile influence function that is independent of surface properties and, after some published and unpublished corrections, made equal to 0.193 by Raupach (1994).

Finally, when reworking all the profile and drag coefficient equations in Andreas (1995) we arrive at his Eq. 29, which conveniently relates drag coefficients at the reference height 10 m to those at height H

$$C_{D10}^{-1/2} = C_{DH}^{-1/2} + \frac{1}{k}\left[\ln\left(\frac{10-d}{H-d}\right) - \psi_H\right]. \tag{13}$$

It remains to determine a value for d that was defined by Thom (1971) as the effective level at which the roughness elements absorb the momentum being transferred to the surface. Raupach (1994) used this definition to derive

$$d = \left(\frac{H\lambda C_R}{C_{SH} + \lambda C_R}\right)\left[1 - c_d C_{DH}^{1/2} A^{1/2}/H\right] \tag{14}$$

with c_d a constant determined by Raupach (1992) to be 0.6 and $A^{1/2}$ is an estimate for the typical streamwise inter-element distance.

First, a value for C_{SH} is computed using the outcome of Eq. 10 as input for Eq. 13. At this point, however, we still do not know a value for d. As in Andreas (1995), d is estimated from using $d/H \approx 0.3$. Iterating the whole set of Equations on d does not give very different results. Considering all uncertainties in the other parameters, this first estimate is very reasonable. Next, we iterate Eq. 9 to obtain C_{DH}. From this we can calculate d from Eq. 14 and then z_0 from Eq. 12.

In Table 3, we summarise the results for z_0 and d using various geometries of the hummocks and domes to illustrate the sensitivity to the input parameters. Values for d are only

Table 3 Aerodynamic roughness lengths (z_0) and displacement heights (d_r, d_a, d_s) for an ice surface covered with hummocks or domes with various geometries

Element type	Height (m)	Radius (m)	z_0 (10^{-3} m)	d_r (m)	d_a (m)	d_s (m)
Hummock	1		13	0.33	0.14	0.11
Hummock	1.5		39	0.66	0.44	0.27
Hummock	2		80	1.04	0.76	0.5
Dome	3	80	2			
Dome	4	80	3			
Dome	3	60	3			
Dome	3	100	2			

The values of z_0 and d_a were calculated with the drag partition model. The values of d_r were calculated with an expression that was derived by Raupach (1994) from results from the same drag model and d_r is calculated with a simple expression that was derived by Shao and Yang (2005) from comparing several drag model results

calculated for hummocks and, to capture the uncertainty of the currently used models, we present results from three different methods. Equation 14 is used to calculate d_a and the simplified expressions from Raupach (1994) and Shao and Yang (2005) yield d_r and d_s, respectively. These are written as

$$\frac{d_r}{H} = 1 - \frac{1 - \exp(-\sqrt{c_{d1}\lambda})}{\sqrt{c_{d1}\lambda}} \tag{15}$$

with parameter $c_{d1} = 7.5$, and

$$\frac{d_s}{H} = \left(\frac{n}{S} bl\right)^k \tag{16}$$

with the term in brackets the so-called skin area index, n/S the unit surface area of a hummock, b and l the width and length of a hummock and $k \approx 0.5$. These are robust expressions that are less sensitive to the choice of model coefficients than the drag model.

The results in Table 3 clearly illustrate that hummocks dominate the total drag of the ice surface at S5. The large-scale terrain roughness (i.e. domes), related to the surface water drainage system, gives values of z_0 that are about one order smaller. The results for hummocks are very sensitive to the height H. Furthermore, varying the slope of the inclined windward directed hummock surface by $\pm$ 25% varies z_0 by about $\pm$ 35%. Notice that the value for z_0, with $H = 1.5$ m, compares well with the results from our measurements at the end of the melt season, giving confidence in the model results. The values for d appear quite sensitive (a factor of 2) to the method used, which illustrates the high uncertainty of the currently available morphometric models. Averaging the results for a hummock with $H = 1.5$ m we estimate that $d \approx 0.5$ m.

Appendix II: Error Analysis

To evaluate the errors in the calculation of z_0 from the profile data we use the general formula for the absolute error ΔX (Fritschen and Gay 1979), which is equivalent to the total differential of the function X consisting of several independent variables y_i, each with its own absolute error Δy_i

$$\Delta X = \frac{\Delta y_1 \partial X}{\partial y_1} + \frac{\Delta y_2 \partial X}{\partial y_2} + \cdots + \frac{\Delta y_n \partial X}{\partial y_n}. \tag{17}$$

We derive a relationship for $\ln(z_0)$ by applying Eq. 1 at two different measurement heights

$$\ln(z_0) = -\ln\left(\frac{z_2'}{z_1'}\right)\frac{U}{\mathrm{d}U} - \frac{\alpha_m \mathrm{d}z U}{z'\mathrm{d}U} z/L_P + \ln(z') + \alpha_m z/L_P \tag{18}$$

with $z_1' = z_1 + d$, $z_2' = z_2 + d$, $z' = z + d$, $\mathrm{d}U = U_2 - U_1$, $\mathrm{d}z = z_2 - z_1$, and $\alpha_m = 5$. The indices 1 and 2 refer to the lower and upper measurement levels at the AWS, respectively. The values for z'/L are directly calculated from Ri_g derived from our two-level AWS data by using Equation 2, hence, $z'/L = z/L_P$. The variables in Eq. 18 that have substantial errors are the displacement height (d), the static stability correction (z/L_P), and the wind gradient ($\mathrm{d}U$). Notice, that the calculation of z/L_P only implies knowledge of the height difference between the measurements and is therefore not affected by errors in d.

The contribution of the aforementioned variables to the error in $\ln(z_0)$ can be found by taking the partial derivatives of Eq. 18 and multiplying these with their respective absolute errors. The errors in U, $\mathrm{d}z$, and α_m are relatively small and neglected here. The partial derivatives for d, z/L_P, and $\mathrm{d}U$ are

$$\frac{\partial(\ln(z_0))}{\partial d} = \left(\frac{1}{z_1'} - \frac{1}{z_2'}\right)\frac{U}{\mathrm{d}U} + \frac{5\mathrm{d}z U}{\mathrm{d}U z'^2} z/L_P + \frac{1}{z'}, \tag{19}$$

$$\frac{\partial(\ln(z_0))}{\partial(z/L_P)} = -\frac{5\mathrm{d}z}{z'}\frac{U}{\mathrm{d}U} + 5, \tag{20}$$

$$\frac{\partial(\ln(z_0))}{\partial(\mathrm{d}U)} = \ln\left(\frac{z_2'}{z_1'}\right)\frac{U}{\mathrm{d}U^2} + \frac{5\mathrm{d}z}{z'}\frac{U}{\mathrm{d}U^2} z/L_P. \tag{21}$$

The errors in d, z/L_P, and $\mathrm{d}U$ are determined to be $\Delta d = 0.5\,\mathrm{m}$, $\Delta(\mathrm{d}U) = 0.1\,\mathrm{m\,s^{-1}}$, and $\Delta(z/L_P) = 0.5 z/L_P$, respectively. Notice, that the uncertainties in d and z/L_P are chosen to be extreme. The error in zL_P equals the envelope of all the scatter in Fig. 7a and Δd is approximately equal to the difference between the minimum and maximum values given in Table 3 of Appendix I.

The method described above gives a maximum possible error estimate since we combine the individual errors in all variables in the most unfavourable way. It is more likely that errors in the various variables are normally distributed, and there is some probability that errors in the different variables will tend to compensate each other to a limited degree. This so-called probable error is calculated from taking the square root of the sum of the squared terms in Eq. 17 (Fritschen and Gay 1979).

Results from both methods are presented in Fig. 12 together with the bin-averaged results for z_0 from S5 (black dots and thick line). The black vertical error bars are the two-sided standard deviations for all data within a bin. The results from the error analysis are all presented single sided, i.e., the results from the absolute and probable error analysis are plotted above and below the black median value line, respectively. The absolute error in $\ln(z_0)$, resulting from the sum of errors in zL_P and d, is plotted as a grey area and that from the wind gradient as a thin black line. The thin dashed black line represents the probable error estimate from all errors.

During winter, $\mathrm{d}U$ leads to a much larger error in $\ln(z_0)$ than d and zL_P. The surface is smooth and, as a consequence, the wind gradient is small, $\Delta(\mathrm{d}U)$ relatively large and $d = 0\,\mathrm{m}$. The increase of the absolute error from z/L_P during winter is a coincidence and indicates larger values of z/L_P in the second half of winter. During the melt season, the error due to d gradually increases to its maximum while the relative importance of $\Delta(\mathrm{d}U)$

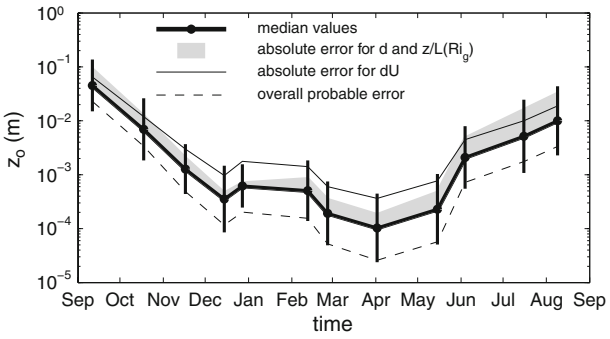

Fig. 12 Profile-derived aerodynamic roughness lengths z_0 from S5 as a function of time plotted together with the results from an error analysis. Every black dot represens the bin-averaged median value (bin size = 25 days) and the black error bars are the twofold standard deviations from the measured data within a bin. The grey colored area represents the sum of absolute errors due to uncertainties in d and z/L_P. The thin black solid line represents the absolute error due to uncertainties in the measurement of the wind gradient and the dashed black line represents the overall probable error

decreases as the surface becomes rougher and dU increases. Remember that these results are obtained by assuming a small value for the measurement error in the wind gradient, $\Delta(\mathrm{d}U) = 0.1\,\mathrm{m\,s^{-1}}$ and, on the other hand, an unlikely large uncertainty for d and z/L_P. Hence, z_0 is most sensitive to measurement errors in the wind gradient and the assumptions made to derive d and z/L_P are relatively unimportant. Only in the case of a very rough surface, such as at S5 at the end of the melt season, are the errors resulting from uncertainties in z/L_P and d of comparable magnitude.

The probable error estimates in Fig. 12 (dashed line) compare very well with the vertical error bars. The occasions that the error bars are larger than the probable error estimates relate to increased variability of z_0 within a bin due to snow events. This variability is not included in the error analysis. Given the sensitivity of z_0 to errors in the wind gradient, the results suggest that the measurement error in the wind gradient is not larger than $\Delta\mathrm{d}U = 0.1\,\mathrm{m\,s^{-1}}$. The wind speed data from the AWS are thus of very good quality throughout the year.

References

Alley RB, Clark PU, Huybrechts P, Joughin I (2005) Ice-sheet and sea-level changes. Science 310:456–460

Ambach W (1977a) Untersuchungen zum energieumsatz in der ablationszone des grönländischen inlandeis, expedition glaciologique internationale au groenland. Bianco Lunos Bogtryyeri A/S, Kobenhagen 4(5):63

Ambach W (1977b) Untersuchungen zum energieumsatz in der akkumulationszone des grönländischen inlandeis, expedition glaciologique internationale au groenland. Bianco Lunos Bogtryyeri A/S, Kobenhagen 4(7):44

Andreas EL (1995) Air-ice drag coefficients in the western weddell sea. 2. A model based on form drag and drifting snow. J Geophys Res 100(C3):4833–4843

Andreas EL (2002) Parameterizing scalar tranfer over snow and ice: a review. J Hydrol 3:417–432

Andreas EL, Claffey KJ (1995) Air-ice drag coefficients in the western weddell sea. 1. Values deduced from profile measurements. J Geophys Res 100(C3):4821–4831

Andreas EL, Lange MA, Ackley SF, Wadhams P (1993) Roughness of weddel sea ice and estimates of the air-ice drag coefficients. J Geophys Res 98:12,439–12,452

Banke E, Smith S, Anderson R (1980) Drag coefficients at aidjex from sonic anemometer measurements. In: Pritchard R (ed) Sea ice processes and models. University of Washington Press, pp 430–442

Blackader AK, Tennekes H (1968) Asymptotic similarity in neutral barotropic boundary layers. J Atmos Sci 25:1015–1020
Box J (2002) Survey of greenland instrumental temperature records. Int J Clim 22:1828–1847
Businger JA, Wyngaard JC, Izumi Y, Bradley EF (1971) Flux-profile relationships in the atmospheric boundary layer. J Atmos Sci 30:788–794
Castro IP, Cheng H, Reynolds R (2006) Turbulence over urban-type roughness: deductions from wind-tunnel measurements. Boundary–Layer Meteorol 118:109–131
Coceal O, Thomas TG, Belcher SE (2007) Spatial variability of flow statistics within regular building arrays. Boundary–Layer Meteorol 125:537–552
Crawley DM, Nickling WG (2002) Drag partition for regularly-arrayed rough surfaces. Boundary–Layer Meteorol 107:445–468
Denby B, Smeets CJPP (2000) Derivation of turbulent flux profiles and roughness lengths from katabatic flow dynamics. J Appl Meteorol 39:1601–1612
Duynkerke PG, Van den Broeke MR (1994) Surface energy balance and katabatic flow over glacier and tundra during GIMEX-91. Glob Planet Change 9:17–28
Forrer J, Rotach MW (1997) On the turbulence structure in the stable boundary layer over the greenland ice sheet. Boundary–Layer Meteorol 85:111–136
Fritschen LJ, Gay LW (1979) Environmental instrumentation. Springer-Verlag, New York 216 pp
Grimmond CSB, Oke TR (1999) Aerodynamic properties of urban areas derived from analysis of surface form. J Appl Meteorol 38:1262–1292
Heinemann G (1999) The KABEG'97 experiment: an aircraft-based study of katabatic wind dynamics over the greenland ice sheet. Boundary–Layer Meteorol 93:75–116
Heinemann G, Falk U (2002) Surface winds and energy fluxes near the greenland ice margin. Polarforchung 71:15–31
Jackson BS, Carroll JJ (1978) Aerodynamic roughness as a function of wind direction over asymmetric surface elements. Boundary–Layer Meteorol 14:323–330
Jacobs AFG, McNaughton KG (1994) The excess temperature of a rigid fast–response thermometer and its effects on measured heat flux. J Atmos Oceanic Technol 11(3):680–686
Joffre SM (1982) Momentum and heat transfers in the surface layer over a frozen sea. Boundary–Layer Meteorol 24:211–229
Kaimal J, Finnigan J (1994) Atmospheric boundary layer flows, 1st edn. Oxford University Press, Cambridge atmospheric and space science series, New York 289 pp
Langleben MP (1974) On wind profiles over sea ice (and discussion with c. a. paulson and n. understeiner). Geophys Res Lett 1:82–85, 313–315
Makin VK, Kudryavtsev VN (1999) Coupled sea surface-atmosphere model, 1, wind over waves coupling. J Geophys Res 104(C4):7613–7623
Meesters AGCA, Bink NJ, Vugts HF, Cannemeijer F, Henneken EAC (1997) Turbulence observations above a smooth melting surface on the greenland ice sheet. Boundary–Layer Meteorol 85:81–110
Moore CJ (1986) Frequency response corrections for eddy correlation's systems. Boundary–Layer Meteorol 37:17–35
Munro DS, Davies JA (1978) On fitting the log-linear model to wind speed and temperature profiles over a melting glacier. Boundary–Layer Meteorol 15:423–437
Oerlemans J, Vugts HF (1993) A meteorological experiment in the melting zone of the greenland ice-sheet. Bull Amer Meteorol Soc 74(3):355–365
Owen PR (1964) Saltation of uniform grains in air. J Fluid Mech 20:225–242
Pandolfo JP (1966) Wind and temperature for constant flux boundary layers in lapse conditions with a variable eddy conductivity to eddy viscosity ratio. J Atmos Sci 23:495–502
Raupach MR (1992) Drag and drag partition on rough surfaces. Boundary–Layer Meteorol 60:375–395
Raupach MR (1994) Simplified expressions for vegetation roughness length and zero–plane displacement as functions of canopy height and area index. Boundary–Layer Meteorol 71:211–216
Raupach MR, Thom AS, Edwards I (1980) A wind–tunnel study of turbulent flow close to regular arrayed rough surfaces. Boundary–Layer Meteorol 18:373–397
Rignot E, Kanagaratnam P (2006) Changes in the velocity structure of the greenland ice sheet. Science 311(5763):986–990
Schotanus P, Nieuwstadt FTM, de Bruin HAR (1983) Temperature measurement with a sonic anemometer and its application to heat and moisture fluxes. Boundary–Layer Meteorol 26:81–93
Shao Y, Yang Y (2005) A scheme for drag partition over rough surfaces. Atmos Environ 39:7351–7361
Smeets CJPP, Duynkerke PG, Vugts HF (1998) Turbulence characteristics of the stable boundary layer over a mid-latitude glacier. part I: a combination of katabatic and large-scale forcing. Boundary–Layer Meteorol 87:117–145

Smeets CJPP, Duynkerke PG, Vugts HF (1999) Observed wind profiles and turbulence fluxes over an ice surface with changing surface roughness. Boundary–Layer Meteorol 92:101–123
Steffen K, Box J (2001) Surface climatology of the greenland ice sheet: greenland climate network 1995–1999. J Geophys Res 106(D24):33,951–33,964
Thom AS (1971) Momentum absorbtion by vegetation. Quart J Roy Meteorol Soc 97:414–428
Velicogna I, Wahr J (2006) Acceleration of greenland ice mass loss in spring 2004. Nature 443:329–331
Van den Broeke MR (1996) Characteristics of the lower ablation zone of the west greenland ice sheet for energy-balance modelling. Annals Geophysica 23:160–166
Van den Broeke MR, Duynkerke PG, Oerlemans J (1994) The observed katabatic flow at the edge of the greenland ice sheet during GIMEX-91. Global Planetary Change 9:3–15
Van de Wal RSW, Greuell MR, van den Broeke MR, Reijmer CH, Oerlemans J (2005) Surface mass balance observations and automatic weather station data along a transect near kangerlussuaq, west greenland. Ann Glaciol 42:311–316
Wieringa J (1993) Representative roughness parameters for homogeneous terrain. Boundary–Layer Meteorol 63:323–363
Wilczak JM, Oncley SP, Stage SA (2001) Sonic anemometer tilt correction algorithms. Boundary–Layer Meteorol 99:127–150